



Interfacial engineering of Ni-phytate and $Ti_3C_2T_x$ MXene-sensitized TiO_2 toward enhanced sterilization efficacy under 808 nm NIR light irradiation

Cheng Jin¹, Dengning Sun¹, Zhongti Sun^{*}, Shaosheng Rao, Zirui Wu, Chao Cheng, Lei Liu, Qinjin Liu^{*}, Juan Yang^{*}

School of Materials Science and Engineering, Jiangsu University, Zhenjiang, Jiangsu 212013, PR China



ARTICLE INFO

Keywords:
NIR-responsive
Photodynamic
Photothermal
Sterilization
Hot-electron

ABSTRACT

Constructing a near-infrared (NIR) light-responsive antibacterial material keeps a preferential goal yet a huge challenge. Herein, we controllably manufactured a sandwich architecture comprised of plasmon ($Ti_3C_2T_x$ MXene) and photosensitizer (PANI (Ni-phytate)) locating on wide-bandgap semiconductor (TiO_2), named as PANI/ TiO_2 / $Ti_3C_2T_x$ (PTM), which can achieve bidirectional transfer of hot-electrons under 808 nm NIR light irradiation, significantly augmenting the carrier concentration of TiO_2 surface. The increase of hot-electron concentration not only strengthens the chemical activity through the O_2 uptake simulations by the theoretical investigations, but also elevates the photothermal conversion efficiency up to 43.3 %, which is far superior to other reported photocatalytic-photothermal system. The 808 nm NIR-activated germicide can realize 99.9 % sterilization efficacy against the Escherichia coli (*E. coli*) with the collaboration of photocatalytic and photothermal treatment. This work offered a brand-new idea to construct a NIR-driven antimicrobial material achieving the synergistic interaction of photocatalytic therapy and photothermal therapy.

1. Introduction

Utilization of sunlight for the pathogenic bacteria elimination and wastewater treatment can be used as an ecofriendly, cost-effective, and broad-spectrum modality. This modality can continually mitigate the environmental and economic issues and boosting the public health [1–3]. Photo-responsive sterilization technique is mainly composed of photodynamic therapy (PDT) and photothermal therapy (PTT), which respectively get through the release of reactive oxygen species (ROS) and heating mode to destroy the structure of bacterial membrane and killing germs, avoiding the antibiotic resistance trouble [4–7]. Moreover, the photothermal process under the near-infrared (NIR) light may also expedite the separation and transfer of photogenic carriers, promoting the generation of ROS. Meanwhile, the formation of hot-electrons by the photocatalytic process may also accelerate the heat effect because of the enhanced electron-phonon interactions, thus reaching synchronous disinfection efficacy between PDT and PTT [8,9]. As is known, the NIR light not only accounts for more than a half of (~52 %) solar spectrum, but also deeply penetrates into the tissues with lower damage to normal cells, compared to the ultraviolet (UV) and visible

light [10,11]. Nevertheless, identifying an ideal NIR-driven bactericides with extensive solar-light exploitation for high sterilization efficacy is still an unresolved challenge [12].

Generally speaking, the traditional NIR-driven antibacterial materials have been developed up to now and can be roughly classified into three genres. The first genre is concerning narrow-bandgap semiconductor-based materials (Ag_2S/Ti_3C_2 , Ag_2S/WS_2 , Bi_2S_3/Ti_3C_2 et al.). Whereas, this strategy has the weak redox capacity and low efficiency of electron-hole separation [4,11,13]. The second genre involves the up-conversion material which can transfer NIR lights to UV or visible light. However, they can only absorb specific NIR wavelength, also reducing the utilization of sunlight [14]. The third genre is based on the construction of metal/semiconductor materials. Because of the formation of Schottky barrier, the hot electrons can transfer to CBM of semiconductor, achieving strong redox capacity and photothermal effect, like Au/TiO_{2-x} hybrid material [15–18]. Unfortunately, its practical application is limited by the work functions between semiconductors and metals, and the high price of precious metals (NPs, e.g., Au, Ag, and Pt). [19–21].

Recently, molecular semiconductor systems have entered our field of

* Corresponding authors.

E-mail addresses: ztsun@ujs.edu.cn (Z. Sun), qqliu@ujs.edu.cn (Q. Liu), yangjuan6347@ujs.edu.cn (J. Yang).

¹ These authors contributed equally.

vision. Compared with traditional noble metal systems, such molecular semiconductor systems have lower cost and even stronger light response and absorption capacity than noble metals under NIR lights [22–24]. For example, Ni-phytate (PANI) have obtained a pressing concern to maximize the photo absorption range of semiconductor in the NIR-activated water splitting on account of strong light harvesting and photoactivity in the NIR light region [25,26]. In addition, $Ti_3C_2T_x$ MXene, as a representative member of MXene, is a fascinating photothermal material, considering the localized surface plasmon resonance (LSPR) effect, strong photo absorption and conversion capability in the NIR light range and excellent conductivity. Moreover, its two-dimensional (2D) delaminated nanosheet with surface functional terminates (such as, $-OH$, $-F$, and $-O$) can offer more active sites for the loading of semiconductor [27–30]. Based on our previous work, the partial oxidation of $Ti_3C_2T_x$ MXene can acquire bits of TiO_2 depositing on it to form Schottky junction of $Ti_3C_2T_x/TiO_2$ heterointerface, which can accelerate

photogenic electron-hole pairs separation and transfer due to the tight contact by in-situ constructing, and elevate the disinfection efficiency in the full spectral light range, compared to the isolated $Ti_3C_2T_x$ and TiO_2 [31]. As is well-known, TiO_2 owns high CBM and low VBM in view of wide bandgap of 3.2 eV, offering a large driving force to generate the ROS, as well as other advantages of good biocompatibility, low-cost, and non-toxicity [32–35]. Nevertheless, the NIR-responsive sterilization performance for the ternary composite of PANI and $Ti_3C_2T_x$ coupling with TiO_2 has not yet been realized.

Herein, we have successfully manufactured a PANI/ $TiO_2/Ti_3C_2T_x$ MXene (PTM) ternary composite as NIR-activated bactericide through the electrostatic self-assembly method. The bidirectional Schottky junctions with PANI/ TiO_2 and $Ti_3C_2T_x/TiO_2$ heterointerface were evidenced by the high-resolution transmission electron microscopy (HRTEM), X-ray photoelectron spectroscopy (XPS) and ultraviolet photoelectron spectroscopy (UPS) characterization. *In situ* XPS

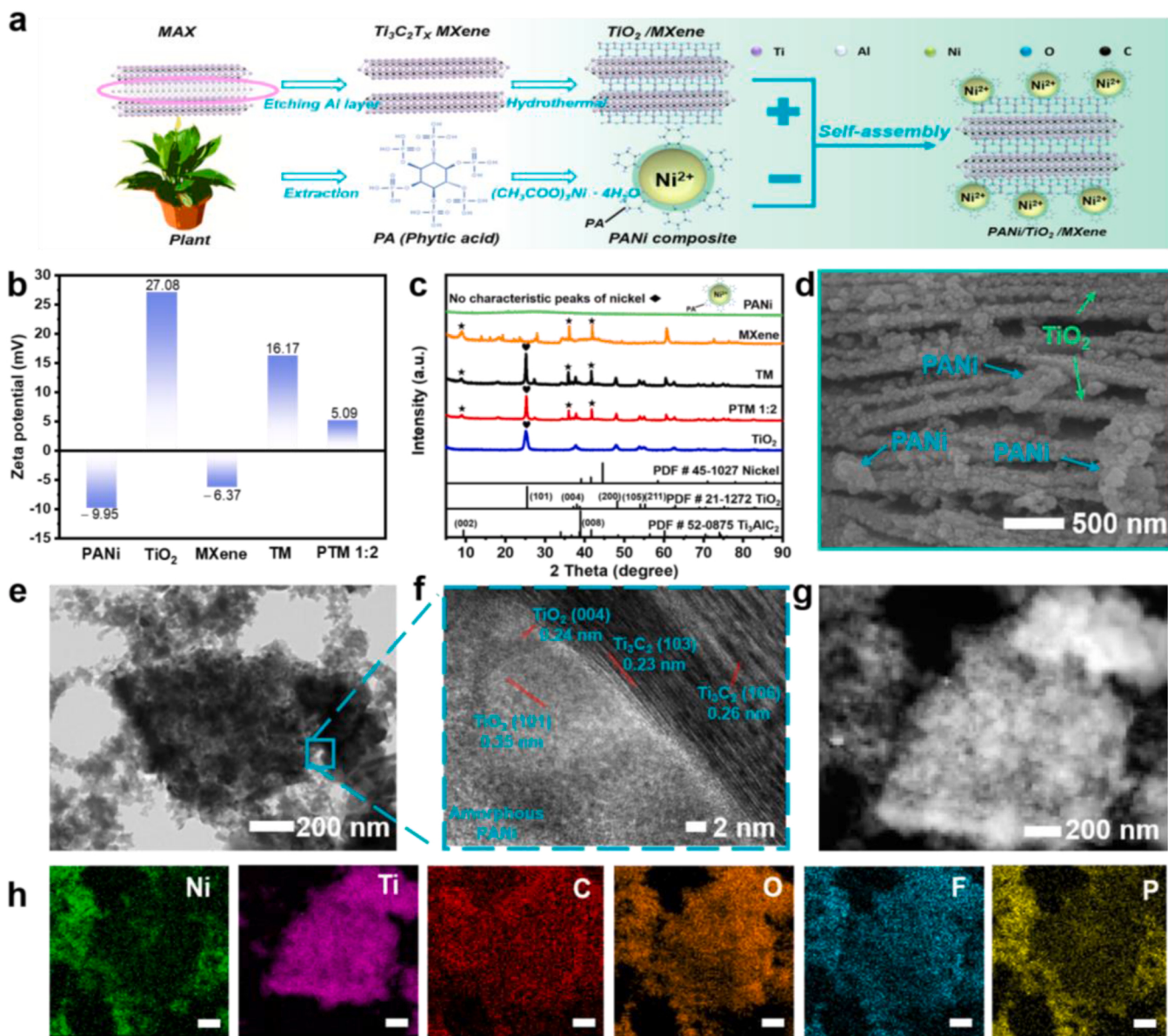


Fig. 1. a) Schematic synthesis process of the PANI/ $TiO_2/Ti_3C_2T_x$ MXene (PTM) photocatalyst; b) The Zeta potentials of thus-fabricated samples; c) X-ray diffraction (XRD) survey of PANI, MXene, TiO_2 , TM and PTM 1:2; d) The scanning electron microscope (SEM) image of PTM 1:2, corresponding the Phytic Acid Nickel Biomimetic Complex (PANI) decorated on the surface labeling by the blue arrows and TiO_2 nanoparticle by the green arrows; e) The transmission electron microscope (TEM) and f) high-resolution TEM (HRTEM) of PTM 1:2; g) High-angle annular dark field scanning transmission electron microscope (HAADF-STEM) image and h) corresponding element mapping of Ni, Ti, C, O, F and P.

technique certified the generation and transfer of hot-electrons from PANi and $Ti_3C_2T_x$ to TiO_2 under the 808 nm NIR light irradiation, and the existence of built-in electric field can effectively suppress the recombination of photogenic carriers, thus enhancing the concentration of hot-electrons in CBM of TiO_2 . Furthermore, DFT simulations indicated the intensive O_2 uptake along with the increase of electron numbers, benefiting for the generation of ROS. The thermal image technique manifested the obvious heat effect with rapid elevation of temperature to about 70 °C within 10 min and the photothermal conversion efficiency of PTM 1:2 can reach up to 43.3 %, superior to other photothermal systems. As a result, the synchronous photocatalytic and photothermal effect can reach 99.9 % sterilization efficacy against the *Escherichia coli* (*E. coli*) under 808 nm NIR light irradiation. This work offers a brand-new attempt for the construction of NIR-responsive germicides, which has the promising potential in the biomedical field.

2. Experimental section

Note that the methods of preparing samples, characterizations and tests, shown in [Supplementary information](#).

3. Results and discussion

Fig. 1a schematically displays the detailed preparation diagram of PTM as photo-driven material, that TiO_2 nanoparticles are in situ derived from $Ti_3C_2T_x$ MXene sheet via hydrothermal method (namely, TM), and then involving the PANi photosensitizer by electrostatic self-assembly on TM with the ratio of PANi:TM in 1:1, 1:2, and 1:3, forming a sandwiched architecture with TiO_2 nanoparticles between PANi and MXene. Note that MXene represents a accordion shape obtained by etching the aluminum layer of the MAX phase. TiO_2 nanoparticles is uniformly grown on MXene nanosheet, benefiting for the interface electron transfer because of tight interaction, as marked in **Fig. S1**. The results of zeta potential for PANi, TiO_2 , MXene, TM and PTM 1:2 samples were also certified the formation of PTM nanocomposites due to electrostatic interactions with positively charged TiO_2 , and negatively charged MXene and PANi in **Fig. 1b**. **Fig. 1c** marks the X-ray diffraction (XRD) patterns of thus-manufactured samples, revealing the crystal composition of PTM 1:2 containing TiO_2 , MXene and PANi phase. Note that PANi has no characteristic peaks of nickel which can be attributed to nickel nanoparticles encapsulated by Phytic acid (PA) [34,35]. **Fig. 1d** shows that TiO_2 nanoparticles are sandwiched between PANi and $Ti_3C_2T_x$ MXene by scanning electron microscope (SEM) image and corresponding element mapping demonstrated in **Fig. S2**. The transmission electron microscope (TEM) and high-resolution TEM (HRTEM) images further show that lattice spacings are 0.23 and 0.26 nm belonging to (103) and (106) crystal planes of $Ti_3C_2T_x$ MXene, 0.25 and 0.24 nm corresponding to (101) and (004) of TiO_2 , and no lattice fringes of PANi in that Ni encased by PA (**Figs. 1e** and **1f**), consistent with XRD survey. In addition, **Fig. 1g** and **1h** can verify the elemental existence and distribution of Ni, Ti, O, C, F, and P, according to high-angle annular dark field scanning transmission electron microscope (HAADF-STEM) and corresponding element mapping images, evidencing the successful preparation of PTM 1:2. To further explore the content of elements, the energy-dispersive X-ray spectroscopy (EDS) result of HAADF-STEM shows that the mass percentage of corresponding element (Ni 6.96 %, Ti 42.99 %, O 28.72 %, C 15.38 %, F 1.19 % and P 4.74 %), matching well with the result of inductively coupled plasma-mass spectrometry (ICP-MS) (Ni 6.51 %) (**Fig. S3** and **Table S1**). Moreover, the SEM, HAADF-STEM, Raman spectra and Fourier transform infrared spectroscopy (FTIR) characterizations for PANi photosensitizer were ulteriorly validate the successful implantation of PANi in the PTM 1:2 photocatalyst, as displayed in **Figs. S4–S9**. This above analysis can provide the successful preparation of PANi and PTM.

The X-ray photoelectron spectroscopy (XPS) and ultraviolet photoelectron spectroscopy (UPS) were used to explore the elemental

composition, valence state of the said samples, energy levels of PANi, TiO_2 and MXene, and ulteriorly confirm charge transfer of PTM 1:2 heterointerface with and without the NIR light. The PTM 1:2 photocatalyst is composed of Ti, C, O, Ni, and P elements through full XPS spectra characterization in **Fig. S10**. The high-resolution Ti 2p XPS spectra of TM and PTM 1:2 can be convoluted into four pairs, including Ti 2p_{1/2} and Ti 2p_{3/2} of TiO_2 , Ti ions with the charged state (Ti_xO_y), Ti–X in titanium carbonate and Ti–C bonds. Among the peaks of TM (458.5 and 461.4 eV) and PTM 1:2 (458.8 and 464.8 eV), corresponding to Ti 2p_{1/2} and Ti 2p_{3/2} of TiO_2 (Ti–O), they all have conspicuous shifts (negative 0.7 and 0.4 eV, and positive 1.0 and 0.8 eV), compared to pure TiO_2 in 457.8 and 464.0 eV, respectively, as displayed in **Fig. 2a** [36]. Besides, the peaks of Ti–C, Ti_xO_y , and Ti–X in TM have apparent negative shifts corresponding to that of pure MXene and the C–Ti of TM has negative shift (0.2 eV) corresponding that of pure MXene, shown in **Fig. S11a and c**. It means that TM and PTM 1:2 exists distinct interface electron transfer from TiO_2 to MXene, generating Schottky junction. The same as the interface between TiO_2 and PANi through the negative shift of P 2p peak from 134.5 eV for Pure PANi to 133.9 eV for PT 1:1 and 133.8 eV for PTM 1:2, as certified by the high-resolution P 2p XPS spectra in **Fig. 2b** and **Fig. S11b**. In addition, the photocurrent response spectroscopy of PT 1:1 and TM are stronger than that of pure TiO_2 , under irradiating with ultraviolet (UV) light, which can indirectly prove the formation of the Schottky junction between TiO_2 and MXene, and TiO_2 and PANi, as shown in **Fig. S12**. Expectedly, the binding energy of divided peaks for Ni 2p spectra in the PANi and PTM 1:2 are no any deviation due to the divalent Ni coordinated with PA molecular in **Fig. 2c**. The high-resolution C 1s and O 1s spectra of PTM 1:2 is also evidenced the formation of PTM 1:2 composite in **Fig. S13**. Under NIR light irradiation, the in-situ XPS Ti 2p_{1/2} and Ti 2p_{3/2} peaks occurs obvious negative shift by 2.7 and 2.5 eV, respectively, as well as the P 2p peak with positive shift of 0.9 eV, compared to the absence of light, manifesting that PANi and MXene can generate hot electrons, transferring to CB of TiO_2 , as displayed in **Figs. 2a** and **2b** [37,38]. It is worth noting that the intensity of peaks about Ti–C, Ti–X and Ti_xO_y obviously weakened, while the intensity of Ti–O (Ti–O) have distinctly enhanced after irradiating with 808 nm NIR light for 30 min. It could be attributed that the generation of hot electrons from MXene and PANi transferring to TiO_2 surface induces the peroxidation of surface groups for MXene (–OH, –F and so on). To further confirm the charge transfer of PTM 1:2 heterointerface when they connected, UPS was executed to survey the work functions of MXene, TiO_2 and PANi compound. The measured secondary electron cutoff energy (E_{cutoff}) of MXene, TiO_2 and PANi were 16.15, 16.48, and 16.30 eV in **Fig. 2d**, corresponding to that of work functions (WFs) with 5.07, 4.74 and 4.92 eV, respectively, based on the equation of $E_{WF} = E_{He\ 1} (21.22\ eV) - E_{cutoff}$ [4,39]. Additionally, the valence band maximum (VBM) position of TiO_2 was 2.52 eV in respect to the fermi level (E_F), namely, –7.26 eV vs. Vacuum energy level. Combined with the E_g of TiO_2 of 3.20 eV, the energy level of conduction band minimum (CBM) is about –4.06 eV (**Fig. S14**). Taken together, the schematic energy level diagrams of MXene, TiO_2 , and PANi phases before contacting are displayed in the **Fig. 2e**. After the generation of bidirectional heterointerfaces, the electrons of TiO_2 spontaneously flowed to MXene and PANi, resulting in positively charged TiO_2 and negatively charged MXene and PANi, also validated by the results of high-resolution Ti 2p and P 2p XPS spectra (**Figs. 2a** and **2b**). As a result, the construction of dual Schottky junctions due to the formation of electron depletion zones in TiO_2 and built-in electric fields is beneficial for the separation of photogenic hot charges at these interfaces of the PTM 1:2 heterojunction, shown in **Fig. 2e** [40,41]. **Fig. 2f** displayed the potential importance of constructing schottky heterojunctions in the condition that semiconductor was not excited under the NIR light [42].

Considering that the light absorption ability is one of the important factors affecting the photocatalytic reaction, the ultraviolet–visible diffuse reflection spectroscopy (UV–vis DRS) spectra of as-prepared samples was used to explore the light absorption of as-prepared

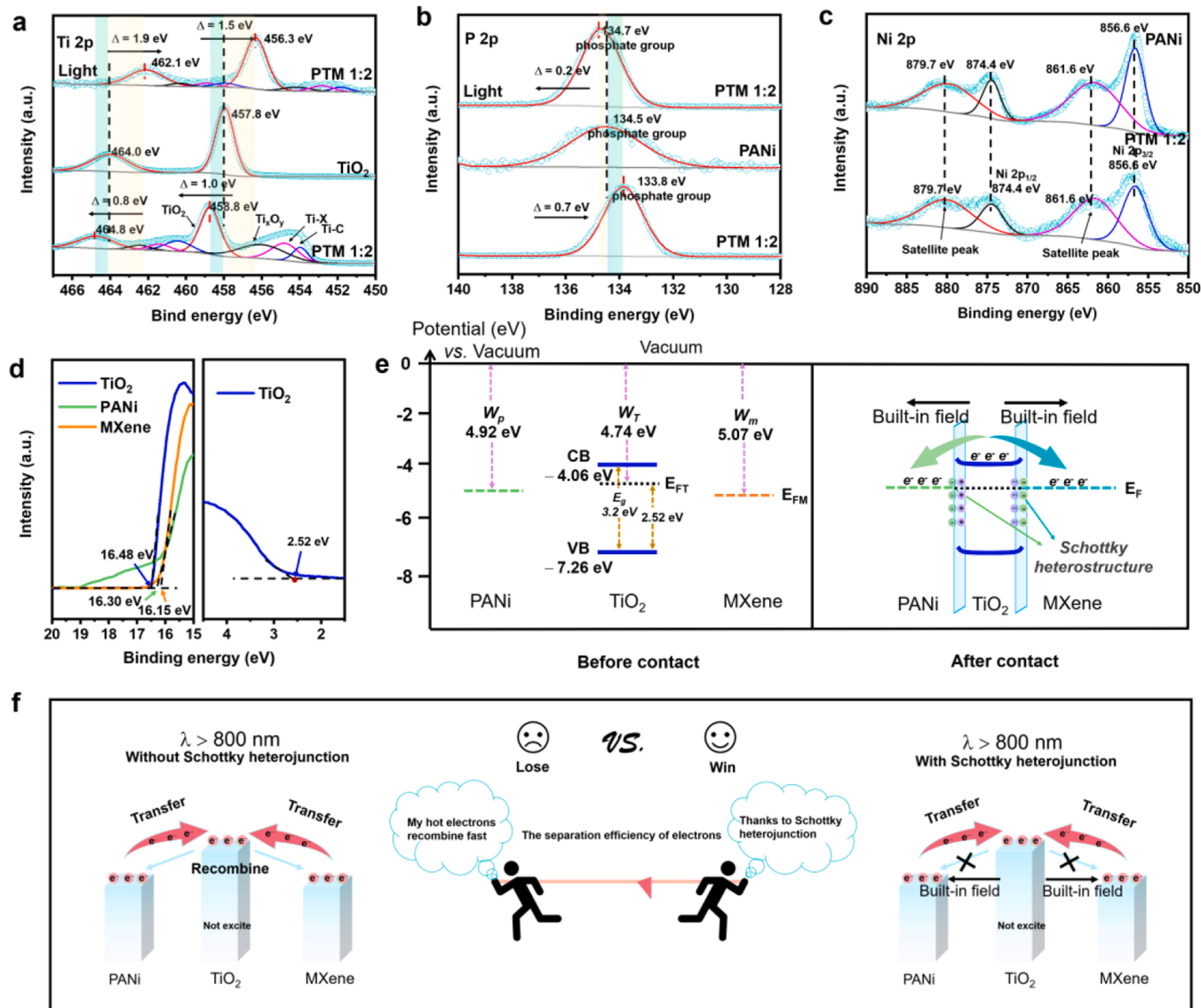


Fig. 2. *In-situ* X-ray photoelectron spectroscopy (in-situ XPS) spectra of a) Ti 2p and b) P 2p of PTM 1:2 with and without light ($\lambda > 800$, 30 min); High-resolution X-ray photoelectron spectroscopy (XPS) spectra of a) Ti 2p, b) P 2p and c) Ni 2p about TiO₂, PANi, and PTM 1:2; d) Ultraviolet photoelectron spectroscopy (UPS) spectra ($h\nu = 21.22$ eV) of MXene, TiO₂ and PANi and the valence band spectrum of TiO₂ with respect to the Fermi level; e) Energy level scheme before and after contact of MXene, TiO₂ and PANi; f) The potential advantage of constructing Schottky heterojunction in a system where semiconductor is not excited under near-infrared light driven system.

samples. As shown in Fig. S14, PTM 1:2 photocatalyst possesses favorable light response capability, indicating that the implantation of MXene and PANi can maximize the light absorbance intensity and absorption range of TiO₂ for the NIR-light driven reaction. In detail, TM sample also has full spectrum photo absorption, mainly ascribing to the incorporation of MXene because of its outstanding light absorption and conversion capability. As expected, the introducing of PANi photosensitizer into TiO₂ may significantly enhance light absorption for the NIR region, specifically for the PT 1:1 composite. Meanwhile, PANi can't alter the intrinsic band gap (E_g) of TiO₂ with 3.20 eV, just acting as a photosensitizer.

To investigate the photo-driving germicidal performance of as-synthesized samples under the 808 nm NIR light, the *Escherichia coli* (*E. coli*), as a representative pathogenic microorganism, is acted as the target object. Initially, the effect of PANi content of PT binary and PTM ternary composite on the antimicrobial activity was researched in Fig. 3a and Fig. S15, the sterilization efficacy was elevated with the increasing ratio of PANi:TiO₂ because of incremental NIR light response

capability to generate more hot electrons, which will be discussed later. Nevertheless, excessive PANi content may also cover more active sites of TM composites, leading to lower biocidal ability, such as, the antibacterial efficiency of PTM 1:1 (83.1 %) is lower than PTM 1:2 (99.9 %), which is higher than PTM 1:3 (80.4 %) due to bits of PANi contents. Thus, it is very imperative to regulate the PANi content of PTM heterostructure in the photocatalytic disinfection. Next, we systematically explore the bactericidal efficacy of ternary PTM 1:2, in combination with the binary TM and PT 1:1, and single-phase MXene and PANi with or without 808 nm NIR light, as shown in Fig. 3b and Fig. S16. Without illumination, the number of colonies were 4.43, 3.45, 3.30, 3.04, 2.99, and $2.64 (\times 10^7 \text{ CFU mL}^{-1})$ for blank, PANi, MXene, TM, PT 1:1, and PTM 1:2 specimens, respectively. After irradiating to 808 nm NIR light, the number of colonies of each sample was tremendously diminished to 3.83, 2.48, 2.03, 1.51, 1.02, and $0.01 (\times 10^7 \text{ CFU mL}^{-1})$, particularly for PTM 1:2 heterostructure. It indicates that the above-mentioned samples are all photo-responsive materials, and the antimicrobial activity of ternary composite PTM 1:2 is distinctly superior to that of binary

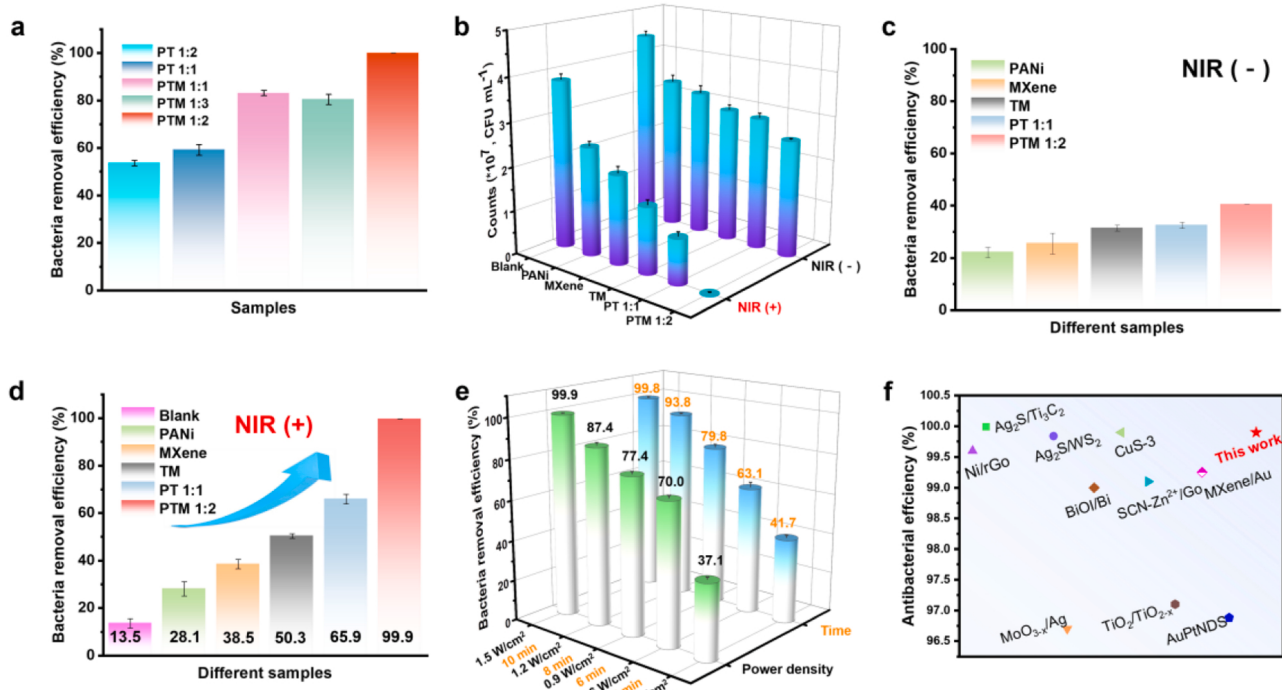


Fig. 3. a) The antibacterial performances of PT 1:2, PT 1:1, PTM 1:1, PTM 1:3 and PTM 1:2 under 808 NIR light (10 min, 200 ppm, 1.5 W cm⁻²); b) Count statistics of different samples under NIR (-) and NIR (+) corresponding spread plate results; Statistical chart of sterilization efficiency for as-synthesized samples under c) NIR (-) and d) NIR (+). (The light source is 808 nm, 1.5 W·cm⁻², the irradiation time is 10 min and the concentration of sample is 200 ppm); e) The antibacterial performances of PTM 1:2 under different power densities and irradiation times; f) The comparisons of the antibacterial efficiencies about different 808 nm NIR-driven sterilization systems.

composites, as well as single phases. The specific mechanism will be explored below. Figs. 3c and 3d displays that the calculated germicidal efficiency of PANi, MXene, TM, PT 1:1, and PTM 1:2 in the dark condition were 22.1 %, 25.5 %, 31.4 %, 32.5 %, and 40.4 %, corresponding to that of irradiation condition were 28.1 %, 38.5 %, 50.3 %, 65.9 % and 99.9 %, respectively, which can confirm the PTM 1:2 heterostructure has excellent bactericidal performance than others under the 808 nm NIR light. Moreover, the disinfection efficacy of PTM 1:2 photocatalyst was dramatically increased following the irradiation time from 2 to 10 min and power intensity from 0.3 to 1.5 W cm⁻², as marked in Fig. 3e, Figs. S17 and S18. In comparison with the different 808 nm NIR-driven sterilization systems, PTM 1:2 ternary composite showed an outstanding antibacterial level, shown in Fig. 3f and Table S2. After photocatalytic bactericidal test, the morphology of *E. coli* turns into shriveled shape from plump rodlike form, as shown in the SEM characterization of Fig. S19. Besides, the XRD pattern, SEM images and TEM images of PTM 1:2 heterointerface has no obvious change before and after exposing to the 808 nm NIR light in Fig. S20, S21 and S22, demonstrating excellent photostability. To investigate which free radicals play a major role in sterilization, 4-hydroxy-2,2,6,6-tetramethylpiperidinyloxy (Tempol) and isopropyl alcohol were used to remove •O₂⁻ and •OH, respectively. Fig. S23 shows that the corresponding sterilization efficiency are 55.4 % and 84.7 %, which represents •O₂⁻ radical plays the major effect. To further verify the real existence of the Schottky heterojunctions in PTM 1:2, we compared the sterilization performance of the PTM 1:2 (99.9 %) with a series of mechanically ground samples (named PTM G1 (55.8 %), PTM G2 (43.1 %) and PTM G3 (33.9 %)) under the same conditions, and the results showed that the PTM 1:2 composite samples prepared by in situ growth method and electrostatic self-assembly method were able to form tight interfaces favorable for electron transfer to form Schottky heterojunctions, which also further proves the real existence of theoretical Schottky heterojunctions from experimental phenomena (Fig. S24). Fig. S25 shows the results of cytotoxicity assay for PTM 1:2

photocatalyst with the different concentration and irradiation time against mouse fibroblasts cells (L929) cells. The PTM 1:2 photocatalyst possesses favorable biocompatibility, despite the increased time and concentration to 24 h and 400 ppm, respectively, the cell viability can achieve to be above 85 %, indicating promising potential in the antibacterial field.

To investigate the photodynamic properties of the aforesaid samples under 808 nm light irradiation, the electron spin resonance (ESR) technique was performed to probe the ROS using 5,5-dimethyl-1-pyrroline N-oxide (DMPO) as a radical capture agent [43]. Figs. 4a and 4b display the ESR signals of DMPO-•O₂ and DMPO-•OH adducts, respectively, the ternary PTM 1:2 composite has strongest intensity of all, indicating favorable capability of ROS release. Specifically, the single-phase MXene and PANi have no obvious signals of DMPO-•O₂ and DMPO-•OH adducts. After coupling with TiO₂, the binary composites PT 1:1 and TM appear evident characteristic peaks of ROS, particularly for the PT 1:1 composite, the intensity is close to the PTM 1:1, demonstrating that the construction of PT interface is more propitious to the release of ROS due to the remarkable transfer of hot-electrons from PANi to TiO₂. Moreover, along with the extension of irradiation time, the ROS contents are significantly augmented in Fig. S26, signifying more hot-electrons assembling on TiO₂ surface for PTM 1:2.

To further clarify the photo-responsive behavior of the foregoing samples under 808 nm NIR light, their photocurrents and electrochemical impedances were characterized in Figs. 4c and 4d. The PTM 1:2 showed maximum photocurrent and minimum impedance than the binary composite and sing-phase. Even though PANi owns barely photoresponsive current, the coupling of TiO₂ dramatically boosts photocurrent and synchronously lessens impedance because the construction of Schottky heterointerface may accelerate the separation of photo-generated electron-hole pairs from PANi photosensitizer, thus transferring to the CB of TiO₂ to form free carriers. However, the integration

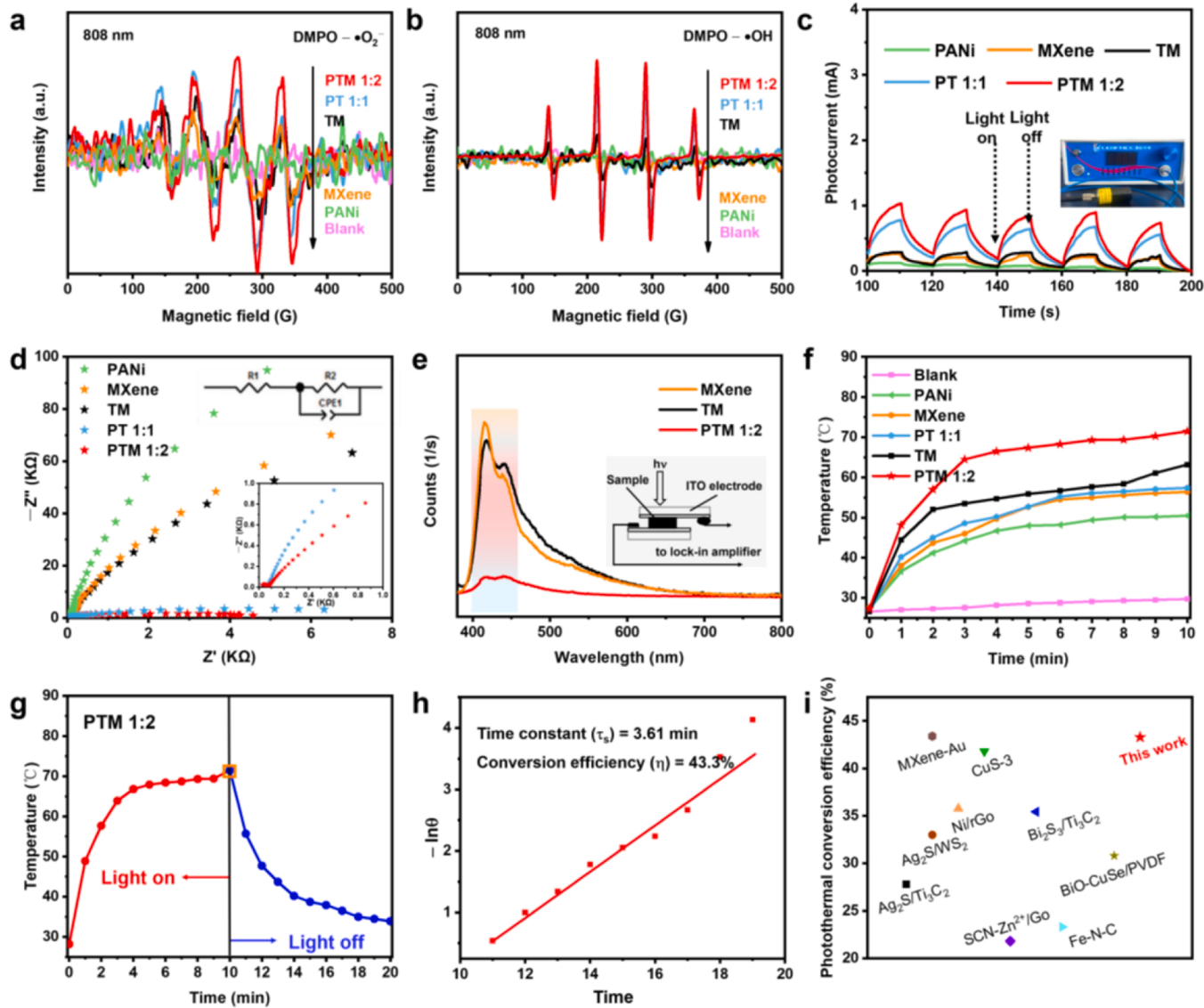


Fig. 4. Electron spin resonance (ESR) signals of a) DMPO- $\cdot\text{O}_2^-$ adducts and b) DMPO- $\cdot\text{OH}$ adducts over Blank, MXene, TM, PT 1:1 and PTM 1:2 under 808 nm light illumination for 10 min; c) Photocurrent response and d) Electrochemical impedance spectroscopy (EIS) Nyquist plots of PANi, MXene, PT 1:1, TM and PTM 1:2 under 808 NIR light; e) Photoluminescence (PL) spectra of MXene, TM and PTM 1:2; f) Photothermal heating curves corresponding to thermal images of different samples under 808 NIR light (The time interval is 1 min). g) Thermal curve of PTM 1:2 (0–10 min exposed to 808 nm NIR light; 11–20 min sheltered to the light). h) Linear relationship between cooling time and τ_s calculated by the cooling period of part for the PTM 1:2; i) The comparisons of photothermal conversion efficiencies of different researches about 808 nm NIR-driven sterilization. Note that the material concentration used in the photothermal test is 200 ppm and the power density is 1.5 W cm⁻².

of MXene and TiO₂ cannot obviously impede the recombination of photogenic carriers. It was supported by the results of photoluminescence (PL) spectra that MXene and TM possess similar PL intensity, but all higher than PTM 1:2 in Fig. 4e [44]. It means that PTM 1:2 heterostructure can remarkably expedite the separation of photo-generated electron-hole pairs, mainly attributed by the establishment of Schottky junction from PANi and TiO₂.

Furthermore, the relationship between the temperature and irradiation time under 808 nm NIR irradiation was recorded in Fig. 4f and Fig. S27. As expected, PTM 1:2 ternary composite has excellent photothermal property that the temperature can quickly reach 65 °C within 3 min and then laxly rise to 70 °C as the time increases to 10 min. Additionally, the single-phase MXene and binary TM all possess higher photothermal temperature than PANi and PT 1:1 composite owing to the LSPR effect of MXene. Hence, the origin of photothermal performance in the PTM 1:2 is mainly contributed by the interface between MXene and

TiO₂. As shown in Fig. 4g and Fig. S28, with or without 808 nm NIR light illumination, the temperature of phosphate buffered saline (PBS) with PTM 1:2 exhibits a on-off effect. Fig. 4h displays the linear regression curve about the negative natural logarithm and cooling time in the cooling stage, the calculated time constant (τ_s) was determined to be 3.61 min, and corresponding photothermal conversion efficiency (η) of PTM 1:2 reached to be 43.3 % (details in Supplementary Information) [11,45,46], which is higher than that of other 808 nm NIR-driven disinfection system (Fig. 4i and Table S3). Additionally, the contribution of antibacterial performance from the ROS release was also measured, the photocatalytic sterilization efficiency is about 41.5 % in Fig. S29. Nevertheless, the total disinfection efficacy (99.9 %) is much larger than the addition of unmixed photothermal (46.3 %) and photocatalytic (41.5 %) efficacy, indicating synergistic bacteria inactivation mechanism.

To ulteriorly demystify the effect of the concentration of hot-

electrons on the generation of ROS at the atomic level, the first-principles method was executed to simulate the capture of reactive species, taking the formation of O_2^- as an example. A series of electrons were considered to insert into the TiO_2 (101) surface, containing 0.1, 0.3, 0.5, 0.7, and 0.9 e^- . In the neutral system, the O_2 molecule physically adsorbed on the TiO_2 (101) surface with an inclined pattern, the bond length of O–O is 1.233 Å, approaching to that of free state O_2 . Following the introducing of electron from 0.1 to 0.9 e^- with the interval of 0.2 e^- , the O–O bond length was continually stretched, corresponding the Ti–O bond length reduced in Fig. 5a, indicating that O_2 molecule was gradually activated, making for the generation of O_2^- . Naturally, the adsorption energies of O_2 molecule were also increased from 0.15 eV on the neutral state to 0.71 eV on the 0.9 e^- state, and corresponding charge numbers of adsorbed O_2 species were also augmented from -0.003 to -0.565 e^- through Bader charge analysis in Fig. 5b. Differential charge density analysis also demonstrated the adsorbed O_2 molecule obtained more electrons from Ti atom serving as active site along with the augmented charge in the composites in Fig. 5c, benefiting for the formation of O_2^- .

Accordingly, the following sterilization mechanism was proposed and schematically displayed in Fig. 5d. The pristine PANi and $\text{Ti}_{3}\text{C}_2\text{T}_x$ MXene only exhibits low photocatalytic and photothermal properties under the 808 nm NIR light irradiation. TiO_2 cannot produce ROS because non-photogenerated electrons were excited by NIR light with

large band-gap (3.2 eV). After the contact between TiO_2 and MXene, TiO_2 and PANi, dual Schottky junctions can be formed at the TiO_2 /MXene and PANi/ TiO_2 heterointerface owing to the difference of WF values. Under the 808 nm NIR illumination, more photogenic electrons derived from PANi and MXene can be rapidly transfer to TiO_2 surface. Then the decreased interface impedance and occurrence of built-in field can be favorable for the transition of photoexcited charges, thus boosting the separation of photogenerated electrons and holes, specifically for the TiO_2/PANI side of PTM ternary composites. Therefore, the formation of ROS is mainly attributed by the involvement of PANi into TiO_2 , manifesting photocatalytic effect. Due to the distinct LSPR of MXene, the $\text{TiO}_2/\text{MXene}$ interface of PTM chiefly dedicates the producing of heat via photothermal process, elevating the temperature. Simultaneously, higher temperature may also lead to chemical reactivity, further promoting the generation of ROS. In the same way, more hot carriers may also result in crystal lattice vibrations, and then boosting the temperature. Hence, the construction of ternary PTM composites comprised by double Schottky junctions can achieve the synergetic photocatalytic and photothermal effect.

4. Conclusion

In conclusion, we successfully fabricated a ternary composite PTM with wide-bandgap semiconductor TiO_2 sandwiching into the

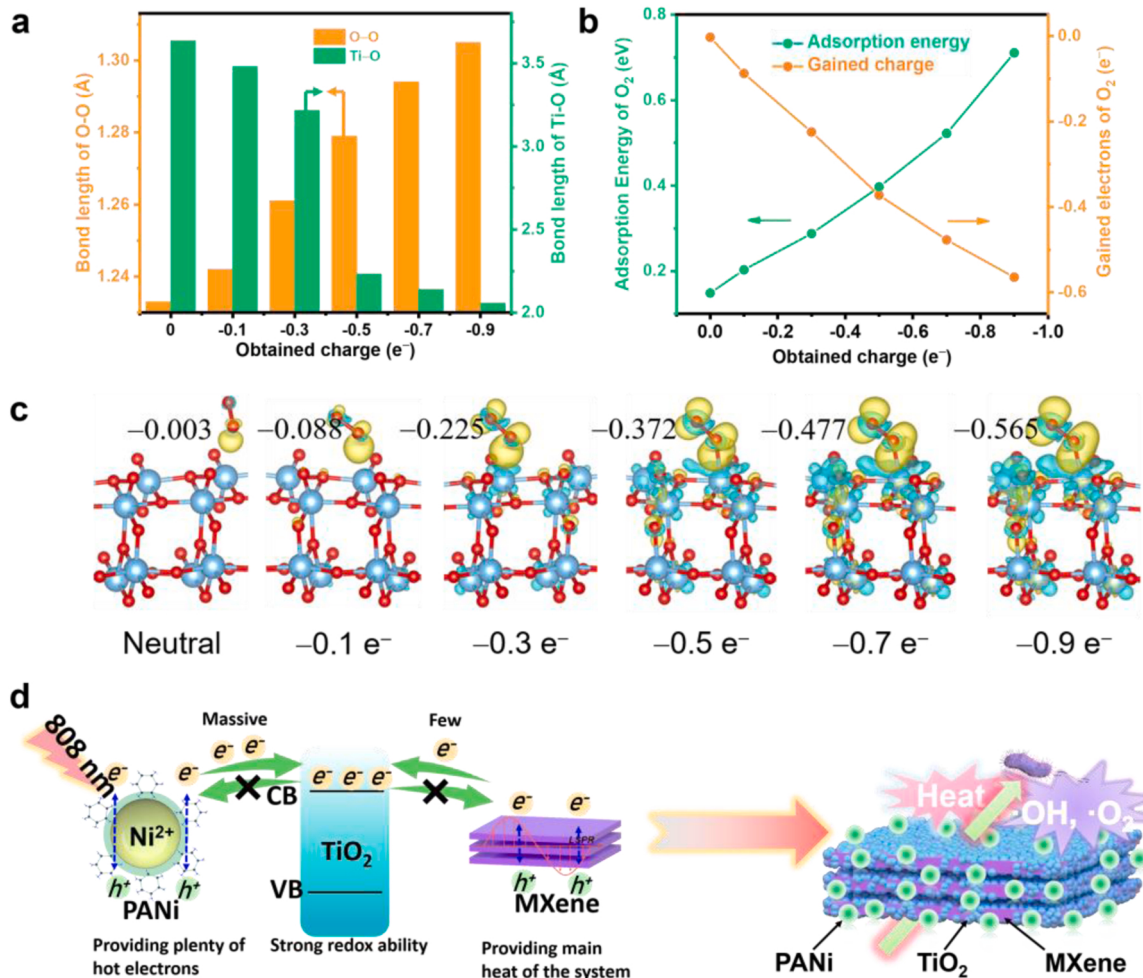


Fig. 5. a) The statistical histogram between O–O bond length of adsorbed O_2 and inserted electrons, the bond length of Ti and adjacent O from O_2 and inserted electrons. b) The relationship between O_2 adsorption energy, obtained charge of adsorbed O_2 and inserting electrons. c) Differential charge density contour of adsorbed O_2 on the TiO_2 (101) in the different inserting electrons from 0 to 0.9 e^- , the yellow and cyan contour with the isosurface value of $0.003 \text{ e}/\text{bohr}^3$ indicates augmented and reduced charge density, respectively. Blue and red ball marks Ti and O atom, respectively. d) Sterilization mechanism of PTM under NIR light (808 nm) irradiation.

photosensitizer PANi and plasmon $Ti_3C_2T_x$ MXene, which exhibits excellent 808 nm NIR-driven antibacterial performance. This dual Schottky junctions offered bidirectional separation and transfer of hot-electrons, further enhancing the redox capability of TiO_2 . The increased carrier concentration not only made for the O_2 capture to produce more ROS, but also gave rise to the release of heat by plasmon $Ti_3C_2T_x$, synchronously achieving the photocatalytic and photothermal treatment. The optimal germicide can realize 99.9 % sterilization efficacy against *E. coli* and the photothermal conversion efficiency reach up to 43.3 % under 808 nm NIR light irradiation, far superior to other photocatalytic-photothermal system. This work offers a novel solution to design NIR-activated bactericidal material using plasmon and photosensitizer coupling wide-bandgap semiconductor, realizing synergistic photocatalytic and photothermal therapy.

CRediT authorship contribution statement

Cheng Jin: Experiments, Investigation, Writing – original draft, Visualization. **Dengning Sun:** Calculation. **Zhongti Sun:** Conceptualization, Writing – review & editing. **Shaosheng Rao:** Writing – review & editing. **Zirui Wu:** Investigation. **Chao Cheng:** Investigation. **Lei Liu:** Biological test. **Qinqin Liu:** Experimental method. **Juan Yang:** Supervision, Project administration, Funding acquisition.

Declaration of Competing Interest

The authors declare that they have no known competing financial interests or personal relationships that could have appeared to influence the work reported in this paper.

Data availability

Data will be made available on request.

Acknowledgements

This work was supported by National Natural Science Foundation of China (No. 51972150, No. 21972058) and Start-up Foundation for Senior Talents of Jiangsu University (No. 21JDG041). The theoretical calculations were performed on A6 Zone of the Beijing Super Cloud Computing Center, supported by PARATERA.

Appendix A. Supporting information

Supplementary data associated with this article can be found in the online version at [doi:10.1016/j.apcatb.2023.122613](https://doi.org/10.1016/j.apcatb.2023.122613).

References

- [1] Y.W. Ren, H.P. Liu, X.M. Liu, Y.F. Zheng, Z.Y. Li, C.Y. Li, K.W.K. Yeung, S.L. Zhu, Y.Q. Liang, Z.D. Cui, S.L. Wu, Photoresponsive materials for antibacterial applications, *Cell Rep. Phys. Sci.* 1 (2020), 100245.
- [2] R. Wang, M.S. Shi, F.Y. Xu, Y. Qiu, P. Zhang, K.L. Shen, Q. Zhao, J.G. Yu, Y. F. Zhang, Graphdiyne-modified TiO_2 nanofibers with osteoinductive and enhanced photocatalytic antibacterial activities to prevent implant infection, *Nat. Commun.* 11 (2020) 4465.
- [3] Z.H. Li, J. Wang, R.C. Shen, N. Chen, X.Y. Qin, W.J. Wang, Q. Yuan, Topological radiated dendrites featuring persistent bactericidal activity for daily personal protection, *Small* 17 (2021), 2100562.
- [4] J.F. Li, Z.Y. Li, X.M. Liu, C.Y. Li, Y.F. Zheng, K.W.K. Yeung, Z.D. Cui, Y.Q. Liang, S. L. Zhu, W.B. Hu, Y.J. Qi, T.J. Zhang, X.B. Wang, S.L. Wu, Interfacial engineering of $Bi_2S_3/Ti_3C_2T_x$ MXene based on work function for rapid photo-excited bacteria-killing, *Nat. Commun.* 12 (2021) 1224.
- [5] Q. Xin, H. Shah, A. Nawaz, W. Xie, M.Z. Akram, A. Batool, L. Tian, S.U. Jan, R. Boddula, B. Guo, Antibacterial carbon-based nanomaterials, *Adv. Mater.* 31 (2019), 1804838.
- [6] R.M. Wang, T.P. Lai, P. Gao, H.M. Zhang, P.L. Ho, P.C.Y. Woo, G.X. Ma, R.Y.T. Kao, H.Y. Li, H.Z. Sun, Bismuth antimicrobial drugs serve as broad-spectrum metallo-β-lactamase inhibitors, *Nat. Commun.* 9 (2018) 439.
- [7] D.L. Han, Y.J. Han, J. Li, X.M. Liu, K.W.K. Yeung, Y.F. Zheng, Z.D. Cui, X.J. Yang, Y.Q. Liang, Z.Y. Li, S.L. Zhu, X.B. Yuan, X.B. Feng, C. Yang, S.L. Wu, Enhanced photocatalytic activity and photothermal effects of cu-doped metal-organic frameworks for rapid treatment of bacteria-infected wounds, *Appl. Catal. B Environ.* 261 (2020), 118248.
- [8] X. Jin, Y.H. Xiong, X.Y. Zhang, R.X. Wang, Y.G. Xing, S. Duan, D.F. Chen, W. Tian, F.J. Xu, Self-adaptive antibacterial porous implants with sustainable responses for infected bone defect therapy, *Adv. Funct. Mater.* 29 (2019), 1807915.
- [9] Z. Zhang, J.Y. Sun, X. Chen, G.Z. Wu, Z.G. Jin, D.G. Guo, L. Liu, The synergistic effect of enhanced photocatalytic activity and photothermal effect of oxygen-deficient Ni/reduced graphene oxide nanocomposite for rapid disinfection under near-infrared irradiation, *J. Hazard. Mater.* 419 (2021), 126462.
- [10] D.D. Zhang, F. Peng, J. Tan, Y. Zhang, J.N. Xie, R. Xu, H.H. Du, S. Qian, Y.Q. Qiao, M. Li, X.Y. Liu, Self-assembled ferric oxyhydroxide nanosheet on PEO-coated magnesium alloy with photocatalytic/photothermal antibacterial and enhanced osteogenesis activities, *Chem. Eng. J.* 437 (2022), 135257.
- [11] Y.F. Lin, D.L. Han, Y. Li, L. Tan, X.M. Liu, Z.D. Cui, X.J. Yang, Z.Y. Li, Y.Q. Liang, S. L. Zhu, S.L. Wu, $Ag_2S@WS_2$ heterostructure for rapid bacteria-killing using near-infrared light, *ACS Sustain. Chem. Eng.* 7 (2019) 14982–14990.
- [12] X.Y. Xu, F.T. Luo, W.S. Tang, J.G. Hu, H.B. Zeng, Y. Zhou, Enriching hot electrons via NIR-photon-excited plasmon in WS_2/Cu hybrids for full-spectrum solar hydrogen evolution, *Adv. Funct. Mater.* 28 (2018), 1804055.
- [13] Q. Wu, L. Tan, X.M. Liu, Z.Y. Li, Y. Zhang, Y.F. Zheng, Y.Q. Liang, Z.D. Cui, S. L. Zhu, S.L. Wu, The enhanced near-infrared photocatalytic and photothermal effects of MXene-based heterojunction for rapid bacteria-killing, *Appl. Catal. B Environ.* 297 (2021), 120500.
- [14] L.J. Bai, W.Y. Jiang, C.X. Gao, S.X. Zhong, L.H. Zhao, Z.Q. Li, S. Bai, Facet engineered interface design of $NaYF_4:Yb,Tm$ upconversion nanocrystals on $BiOCl$ nanoplates for enhanced near-infrared photocatalysis, *Nanoscale* 8 (2016) 19014–19024.
- [15] X.D. An, J.C. Kays, L.V. Lightcap, T.H. Ouyang, A.M. Dennis, B.M. Reinhard, Wavelength-dependent bifunctional plasmonic photocatalysis in Au/Chalcocite hybrid nanostructures, *ACS Nano* 16 (2022) 6813–6824.
- [16] P. Yin, J. Yu, L. Wang, J. Zhang, Y. Jie, L.F. Chen, X.J. Zhao, H.S. Feng, Y.S. Yang, M. Xu, X. Zhang, J.B. Han, H. Yan, M. Wei, Water-gas-shift reaction on Au/TiO_{2-x} catalysts with various TiO_2 crystalline phases: a theoretical and experimental study, *J. Phys. Chem. C* 125 (2021) 20360–20372.
- [17] Y.N. Montecelo, A. Movsesyan, J. Gao, S. Burger, Z.M.M. Wang, S. Nlate, E. Pouget, R. Oda, M. Comesana-Hermo, A.O. Govorov, M.A. Correa-Duarte, Chiral generation of hot carriers for polarization-sensitive plasmonic photocatalysis, *J. Am. Chem. Soc.* 144 (2022) 1663–1671.
- [18] H.G. Zhu, X. Yuan, Q.F. Yao, J.P. Xie, Shining photocatalysis by gold-based nanomaterials, *Nano Energy* 88 (2021), 106306.
- [19] S.W. Lee, H. Lee, Y.J. Park, H. Kim, G.A. Somorjai, J.Y. Park, Surface chemistry of hot electron and metal-oxide interfaces, *Surf. Sci. Rep.* 76 (2021), 100532.
- [20] Q.Q. Huang, Z.B. Fang, K. Pang, W.K. Qin, T.F. Liu, R. Cao, The impact of secondary building units in metal-organic frameworks on plasmonic gold-sensitized photocatalysis, *Adv. Funct. Mater.* 32 (2022), 2205147.
- [21] Q.Q. Lang, Y.H. Chen, T.L. Huang, L.N. Yang, S.X. Zhong, L.J. Wu, J.R. Chen, S. Bai, Graphene “bridge” in transferring hot electrons from plasmonic Ag nanocubes to TiO_2 nanosheets for enhanced visible light photocatalytic hydrogen evolution, *Appl. Catal. B Environ.* 220 (2018) 182–190.
- [22] K.F. Yu, P.Y. Jiang, H.B. Yuan, R. He, W.K. Zhu, L.B. Wang, Cu-based nanocrystals on ZnO for uranium photoreduction: plasmon-assisted activity and entropy-driven stability, *Appl. Catal. B Environ.* 288 (2021), 119978.
- [23] G.V. Hartland, L.V. Besteiro, P. Johns, A.O. Govorov, What's so hot about electrons in metal nanoparticles, *ACS Energy Lett.* 2 (2017) 1641–1653.
- [24] H.F. Xiang, J.H. Cheng, X.F. Ma, X.G. Zhou, J.J. Chruma, Near-infrared phosphorescence: materials and applications, *Chem. Soc. Rev.* 42 (2013) 6128–6185.
- [25] Y.Y. Huang, D. Li, S. Feng, Y.J. Jia, S.H. Guo, X.J. Wu, M. Chen, W.D. S, Pt Atoms/Clusters on ni-phytate-sensitized carbon nitride for enhanced NIR-light-driven overall water splitting beyond 800 nm, *Angew. Chem. Int. Ed.* 61 (2022), e202212234.
- [26] Y.Y. Huang, Y.P. Jian, L.H. Li, D. Li, Z.Y. Fang, W.X. Dong, Y.H. Lu, B.F. Luo, R. J. Chen, Y.C. Yang, M. Chen, W.D. Shi, A. NIR-responsive, phytic acid nickel biomimetic complex anchored on carbon nitride for highly efficient solar hydrogen production, *Angew. Chem. Int. Ed.* 60 (2021) 5245–5249.
- [27] Y.H. Chen, M.Y. Qi, Y.H. Li, Z.R. Tang, W. Wang, J.L. Gong, Y.J. Xu, Activating two-dimensional $Ti_3C_2T_x$ -MXene with single-atom cobalt for efficient CO_2 photoreduction, *Cell Rep. Phys. Sci.* 2 (2021), 100371.
- [28] D.Q. Fan, Y. Lu, H. Zhang, H.L. Xu, C.H. Lu, Y.C. Tang, X.F. Yang, Synergy of photocatalysis and photothermal effect in integrated 0D perovskite oxide/2D MXene heterostructures for simultaneous water purification and solar steam generation, *Appl. Catal. B Environ.* 295 (2021), 120285.
- [29] S.Y. Hao, H.C. Han, Z.Y. Yang, M.T. Chen, Y.Y. Jiang, G.X. Lu, L. Dong, H.L. Wen, H. Li, J.R. Liu, L.L. Wu, Z. Wang, F.L. Wang, Recent advancements on photothermal conversion and antibacterial applications over MXenes-based materials, *Nano Micro Lett.* 14 (2022) 178.
- [30] Y.P. Cao, H. Chen, Y.P. Shen, M. Chen, Y.L. Zhang, L.Y. Zhang, Q. Wang, S.J. Guo, H. Yang, SnS_2 Nanosheets anchored on nitrogen and sulfur co-doped MXene sheets for high-performance potassium-ion batteries, *ACS Appl. Mater. Interfaces* 13 (2021) 17668–17676.
- [31] C. Jin, S.S. Rao, J. Xie, Z.T. Sun, J.S. Gao, Y. Li, B. Li, S.W. Liu, L. Liu, Q.Q. Liu, J. Yang, Enhanced photocatalytic antibacterial performance by hierarchical $TiO_2/W_{18}O_{49}$ Z-scheme heterojunction with $Ti_3C_2T_x$ -MXene cocatalyst, *Chem. Eng. J.* 447 (2022), 137369.

- [32] M. Nolan, A. Lwaszuk, A.K. Lucid, J.J. Carey, M. Fronzi, Design of novel visible light active photocatalyst materials: surface modified TiO₂, *Adv. Mater.* 28 (2016) 5425–5446.
- [33] B. He, Z.L. Wang, P. Xiao, T. Chen, J.G. Yu, L.Y. Zhang, Cooperative coupling of H₂O₂ production and organic synthesis over a floatable polystyrene-sphere-supported TiO₂/Bi₂O₃ S-scheme photocatalyst, *Adv. Mater.* 34 (2022), 2203225.
- [34] J.B. Cai, X.Q. Wu, S.X. Li, F.Y. Zheng, Controllable location of Au nanoparticles as cocatalyst onto TiO₂@CeO₂ nanocomposite hollow spheres for enhancing photocatalytic activity, *Appl. Catal. B Environ.* 201 (2017) 12–21.
- [35] J. Wang, X.X. Gao, Y.J. Wang, S.Y. Wang, Z.W. Xie, B.Z. Yang, Z.G. Zhang, Z. Yang, L. Kang, W.Q. Yao, Multifunctional core-double-shell Ce@MnO@TiO₂ catalysts with enhanced full-light conversion for the highly efficient photothermal oxidation of toluene, *Appl. Catal. B Environ.* 317 (2022), 121789.
- [36] K. Rajavel, S.Y. Shen, T. Ke, D.H. Lin, Photocatalytic and bactericidal properties of MXene-derived graphitic carbon-supported TiO₂ nanoparticles, *Appl. Surf. Sci.* 538 (2021), 148083.
- [37] P.F. Xia, S.W. Cao, B.C. Zhu, M.J. Liu, M.S. Shi, J.G. Yu, Y.F. Zhang, Designing a 0D/2D S-Scheme heterojunction over polymeric carbon nitride for visible-light photocatalytic inactivation of bacteria, *Angew. Chem. Int. Ed.* 59 (2020) 5218–5225.
- [38] Q.L. Xu, L.Y. Zhang, B. Cheng, J.J. Fan, J.G. Yu, S-Scheme heterojunction photocatalyst, *Chem* 6 (2020) 1543–1559.
- [39] W.C. Huang, Y. Gao, J.X. Wang, P.C. Ding, M. Yan, F.M. Wu, J. Liu, D.Q. Liu, C. S. Guo, B. Yang, W.W. Cao, Plasmonic enhanced reactive oxygen species activation on low-work-function tungsten nitride for direct near-infrared driven photocatalysis, *Small* 16 (2020), 2004557.
- [40] A.J. Nozik, Utilizing hot electrons, *Nat. Energy* 3 (2018) 170–171.
- [41] B. Jeon, C. Lee, J.Y. Park, Electronic control of hot electron transport using modified schottky barriers in metal–semiconductor nanodiodes, *ACS Appl. Mater. Interfaces* 13 (2021) 9252–9559.
- [42] J.W. Xu, N. Liu, D. Wu, Z.D. Gao, Y.Y. Song, P. Schmuki, Upconversion nanoparticle-assisted payload delivery from TiO₂ under near-infrared light irradiation for bacterial inactivation, *ACS Nano* 14 (2020) 337–346.
- [43] Y. Nosaka, A. Nosaka, Understanding hydroxyl radical (•OH) generation processes in photocatalysis, *ACS Energy Lett.* 1 (2016) 356–359.
- [44] R. Wang, K.Q. Lu, Z.R. Tang, Y.J. Xu, Recent progress in carbon quantum dots: synthesis, properties and applications in photocatalysis, *J. Mater. Chem. A* 5 (2017) 3717–3734.
- [45] Y. Li, X.M. Liu, L. Tan, Z.D. Cui, X.J. Yang, Y.F. Zheng, K.W.K. Yeung, P.K. Chu, S. L. Wu, Rapid sterilization and accelerated wound healing using Zn²⁺ and graphene oxide modified g-C₃N₄ under dual light irradiation, *Adv. Funct. Mater.* 28 (2018), 1800299.
- [46] M.G. Yang, S. Qiu, E. Coy, S.J. Li, K. Załęski, Y. Zhang, H.B. Pan, G.C. Wang, NIR-responsive TiO₂ biometasurfaces: toward in situ photodynamic antibacterial therapy for biomedical implant, *Adv. Funct. Mater.* 34 (2022), 2106314.